Investigation of solute segregation behavior using a correlative EBSD/TKD/APT methodology in a 16MND5 weld

Leifeng Zhang, Bertrand Radiguet, Patrick Todeschini, Christophe Domain, Yang Shen, Philippe Pareige

To cite this version:

Leifeng Zhang, Bertrand Radiguet, Patrick Todeschini, Christophe Domain, Yang Shen, et al.. Investigation of solute segregation behavior using a correlative EBSD/TKD/APT methodology in a 16MND5 weld. Journal of Nuclear Materials, 2019, 523, pp.434-443. ⟨10.1016/j.jnucmat.2019.06.002⟩. ⟨hal-02172714⟩

HAL Id: hal-02172714

https://normandie-univ.hal.science/hal-02172714v1

Submitted on 25 Oct 2021

Investigation of solute segregation behavior using a correlative EBSD/TKD/APT methodology in a 16MND5 weld

Leifeng Zhang[a1], Bertrand Radiguet[a2], Patrick Todeschini[b], Christophe Domain[b], Yang Shen[c], Philippe Pareige[a]

[a] Groupe de Physique des Matériaux, UMR CNRS 6634, Université de Rouen Normandie et INSA de Rouen, 76800 Rouen, France

[b] Département Matériaux et Mécanique des Composants, EDF R&D, Site des Renardières-Ecuelles, 77818 Moret-sur-Loing cedex, France

[c.] LIDEC, Direction Industrielle, EDF DIPNN, 37420 Avoine cedex, France

Abstract

In the present study, a correlative Electron Backscattering Diffraction (EBSD)/Transmission Kikuchi Diffraction (TKD)/Atom Probe Tomography (APT) methodology was used to investigate the solute segregation behavior in a low-alloyed weld. Three dimensional chemical information was correlated to the crystallographic features of Grain Boundaries (GBs). The steel has a complex microstructure of acicular ferrite and intergranular carbides. About 78% High Angle Grain Boundaries (HAGBs, with about 12% Σ3 HAGBs) and about 22% Low Angle Grain Boundaries (LAGBs) were observed. APT analyses revealed the segregation of one element or several chemical species (C, P, Mn, Si, Ni, Cr and Mo) at GBs or carbide-ferrite interfaces. Taking into account the nature of segregants and the five-parameter GB crystallography, both interstitial and substitutional segregation behaviors were discussed. The results reveal a significant influence of misorientation angle (or deviation angle) on interstitial segregation for LAGBs (or Σ3 special HAGBs) and also a

---

1 Corresponding author. E-mail address: WWWXYXY@163.com

2 Corresponding author. E-mail address: bertrand.radiguet@univ-rouen.fr

strong influence of the GB plane on substitutional segregation for Σ3 special HAGBs and general HAGBs.

Key words: Grain boundaries; interfaces; APT; segregation; acicular ferrite; carbide

Graphical abstract

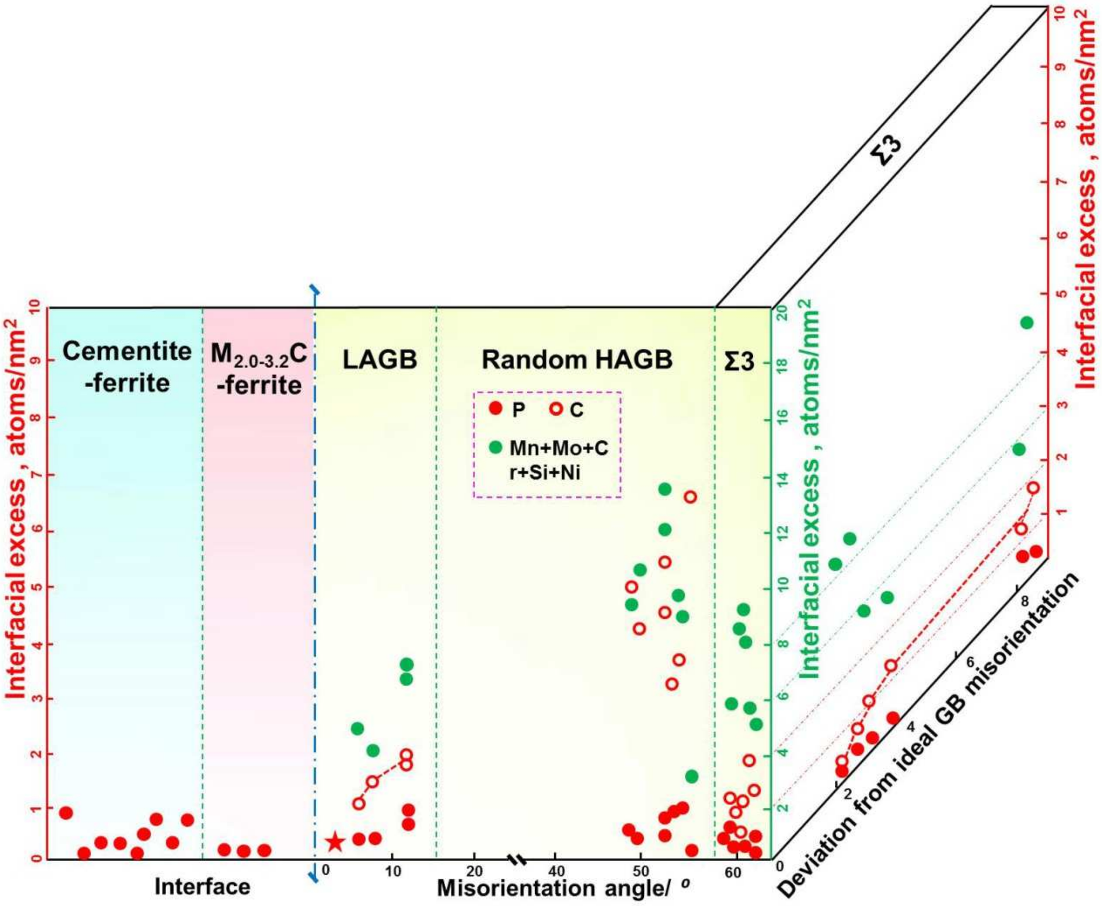

1. Introduction

Solute segregation to GBs may be either beneficial or detrimental for properties [1]. For the past 60 years, GB segregation issue in Reactor Pressure Vessel (RPV) steels and other alloys, in particular the intergranular P segregation, has been intensively studied both experimentally and by modelling as reviewed in literature [2-9]. Experimental research is frequently carried out by Auger Electron Spectroscopy (AES) that requires GBs to be fractured. Analyses are performed on selected “brittle” GBs with a high segregation level [10-13]. AES has a fast acquisition speed to collect the data and a good precision on the composition measurement, but the crystallographic information is lost. Later, a new door has been opened with some advanced techniques, including Analytical Electron Microscopy (AEM) [14, 15] and Atom Probe Field Ion Microscopy (APFIM) [16, 17]. These tools allow a precise measurement of the chemical segregation at the atomic level to be obtained even for non-brittle alloying systems. Transmission Electron Microscopy-Energy Dispersive Spectrometry (TEM-EDS) can provide both crystallographic and chemical information. However, TEM is confined to 2 dimensions, the depth information being difficult to be determined. Electron Energy Loss Spectroscopy (EELS) can provide a wealth of information (for example, concentration, nearest-neighbor atomic structure, local thickness and free-electron density), but the convolution of all the detected information in a single spectrum makes it challenging to quantify absolute values [18]. In contrast, APT is a unique technique in quantifying local chemical composition, offering extensive capabilities for both 3D mapping at fine scale and chemical composition measurements at the atomic scale (atomic resolution in depth and 0.3-1.0 nm laterally) [19]. Particularly, it has strong ability to identify multiple chemical species in one sample with high sensitivity, and its acquisition efficiency as well as detection capacity has been improved [20]. Today, the crystallographic details, as provided by electron microscopies (including TEM [21], EBSD and/or TKD [22-28]), can be correlated to APT data. This has been reviewed in the literature [29].

The improvement of these instruments or the correlative methodologies helps to perform in-depth investigations of GB segregation behavior. As reported in a nanocrystalline material, a correlative TEM/APT approach has established a clear C segregation map in relation with GB misorientation angle [21, 30]. The C segregation level increases with the misorientation angle in the LAGB region. In contrast, there exists a large data scattering in the HAGB region, in which the same misorientation angle may correspond to both high and low segregation levels. For polycrystalline materials with a complex composition, the detailed solute segregation behavior in relation with GB nature was rarely reported.

This paper focuses on a 16MND5 weld, which is produced for RPV, a component acting as a barrier between the primary water and the reactor building. With the intensive expectations for extending the service lifespans of Nuclear Power Plants (NPPs), it is of more and more importance to get a reliable evaluation of the microstructural change and the corresponding property degradation of RPV steels [31]. The RPV steels, subjected to thermal ageing and neutron irradiation, may embrittle gradually during operation [32]. This embrittlement is mainly attributed to a hardening mechanism, related to the formation of Cu-rich [33, 34] and Ni, Mn, Si-rich features [35-37]. These features can pin the dislocations and reduce their mobility, thus enhancing the yield strength. Besides, a non-hardening mechanism, due to intergranular impurity segregation (especially P) that impairs the GB cohesion, could also contribute to the embrittlement [7, 38]. For VVER-1000 RPV welds being exposed at 310-320°C up to 200000 h, the reversible temper brittleness due to the intergranular P accumulation was responsible for thermal ageing effects and a considerable increase of intergranular embrittlement tendency [4]. APT analyses on VVER-1000 base and weld metals revealed an obvious GB segregation of P (and also other alloying elements), but no detailed information on GB features was given [39]. The co-segregation behavior of P and other alloying elements has also been reported in Cr-Mo(-V) steels [40-42]. However, the detailed segregation behavior for all chemical species, especially that with regard to the GB character, remains unclear.

The main aim of this research is to quantify GB segregation in a 16MND5 weld steel. Using the correlative EDSD/TKD/APT methodology [24, 26, 43], the crystallographic information, or the 5 Degrees of Freedom (DOFs), and chemical composition were collected simultaneously. Both the interstitial and substitutional segregations were discussed. The segregation behavior at carbide-ferrite heterophase boundaries was also studied.

2. Experimental method

2.1 Material, sample preparation and experimental conditions

The chemical composition of the 16MND5 weld steel is listed in Table 1. The P content is 80 wt.ppm (or 140 at.ppm). After steelmaking, forging and welding (submerged arc welding), the subsequent stress-relief heat treatment was performed at 595-610°C for 16.5 h, followed by a controlled cooling at 15°C/h down to 350°C and then air cooling to ambient temperature. The microstructure was observed by Scanning Electron Microscopy (SEM) and EBSD in a dual-beam SEM/FIB instrument (Zeiss Nvision 40 with the AZtec acquisition software and XB 540 with the TEAM-EDAX software). Specimens for SEM/EBSD analyses, in the shape of thin slices of $10\times10\times0.3$ mm^3, were cut from as-received half Charpy sample and then fixed into a conductive resin with a diameter of 25 mm. Afterwards, the specimens were ground with coarse, medium and fine sandpaper discs and then polished on special cloths with diamond liquids. The samples were finally polished in a semi-automatic polishing machine for 30 min using a 0.04 μm colloidal silica suspension. Samples for SEM observations were finally chemically etched with 1% Nital solution for 60 s. The EBSD experiments were performed at 20 kV at a working distance of 10 mm, with a step size of 0.1 μm×0.1 μm. Patterns were captured with a 4×4 binning mode on the DigiView 5 camera from EDAX. For statistics, any point pair with misorientation exceeding 2° was regarded as a boundary. Based on Coincidence Site Lattice (CSL) theory in cubic lattice, the GBs, with misorientation characteristics of $60°\langle111\rangle$ considering a tolerance of 8.7° were considered as Σ3 special HAGBs [5]. The tolerance value is defined by K/Σ^n, where K is a constant, Σ value is calculated by the ratio between all sites and coincident sites at the boundary plane. The angular tolerance value is defined according to Brandon Criterion [44], selecting a K value of 15 and a n value of 0.5.

Table 1 Bulk chemical composition of the 16MND5 weld steel

	C	P	Si	Mn	Ni	Cr	Mo	Cu	Fe
wt.%	0.07	0.008	0.43	1.57	0.75	0.16	0.58	0.04	Bal.
at.%	0.34	0.014	0.84	1.60	0.72	0.18	0.34	0.04	Bal.

Fig. 1 depicts the experimental sequence for the detailed site-specific sample preparation, starting from the GB identification in bulk material to the final APT tip, at the apex of which a specific GB was located. In Fig. 1a, after selecting a GB, FIB was utilized to mill trenches (Fig. 1b). As shown in Fig. 1c, a micromanipulator and a Gas Injection System (GIS) were used to lift out the wedge-shaped chunk containing the Region of Interest (ROI), which was subsequently placed on the cap of tungsten pre-tip. During the subsequent annular milling (Fig. 1d), FIB column was used as a milling tool to sharpen the tip at 30 kV, with the beam currents decreasing successively from 700 pA to 40-50 pA. To minimize the Gallium-contaminated layer in the tip, the final cleaning procedure was completed at 2 kV with a current of 100 pA. To ensure the specific GB being located near the apex of the final tip (Fig. 1e), TKD was used during the final steps of annular milling. This is because the imaging contrast in SEM view failed to identify the GB location when the tip was too thin (<300-500 nm). In contrast, TKD technique can help to locate the GB's position during annular milling. The second advantage of using TKD is to obtain the 5 DOFs with the combination of APT 3D reconstruction. The HKL channel 5 software (or the TSL-OIM software) and Carine crystallography software were utilized for the identification of GB crystallography. It should be noticed that, for the GB plane identification, the maximum Miller index values are limited to 6 in these softwares.

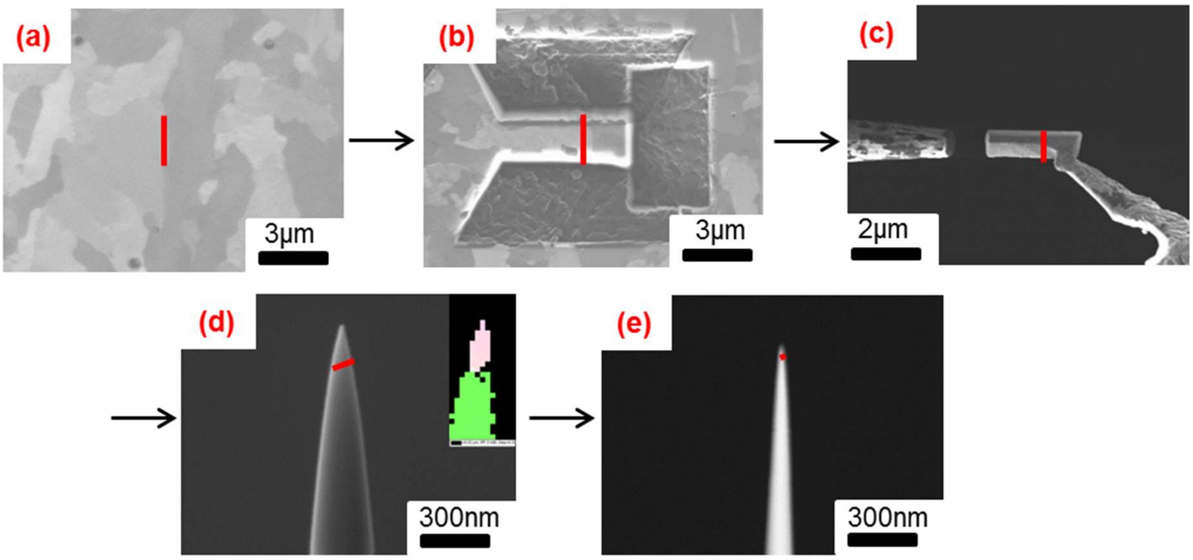

Fig. 1 Steps of sample preparation of an APT needle containing a GB: (a) selection of a ROI containing a specific GB; (b) milling a slice with FIB; (c) lift-out the chunk with a micromanipulator; (d) annular milling with TKD; (e) cleaning with FIB. Note that, the GB location is delineated by a solid red line and in (d), the TKD image showing the distinct contrasts across a GB is placed at the top right area.

Microanalyses were carried out with a Local Electrode Atom Probe (LEAP 4000 XHR, CAMECA) operated at a temperature of 55 K, a detection rate of 0.15%, a pulse repetition rate of 200 kHz and a pulse fraction equal to 20% of the standing voltage. It was reported that some light-weight elements (such as B [45], P [46] and C [47]) may migrate from one place to another (particularly low-index poles) along the tip surface prior to field evaporation. In that case, the observed atomic position in the reconstructed volume may not correspond to the original location in the steel. The enhanced surface migration could be of particular concern for the laser-pulsed mode atom probe where heating effect is more favored [48, 49]. That is why a high-voltage pulse mode was adopted in the present research. The 3D reconstruction procedure for APT data analyses has been stated in relevant literature [50-52]. According to these principles and the visible crystallographic poles from the detector event histogram map, the image compression factor and field factor were determined. Both the commercial IVAS software (CAMECA, v. 3.6.6) and the GPM 3D software (from GPM lab, v. 6.3) were used for data reconstruction.

2.2 Data analyses for GB chemistry and crystallography

2.2.1 Identification of crystallographic detail

Five independent parameters (or 5 DOFs) are required to fully describe the structure of a GB between grains A and B. Three DOFs, including one for misorientation angle θ and two for rotation axis $\boldsymbol{c} = [h_0k_0l_0]$, are used to define the mutual misorientation between the two crystals, and two DOFs are applied to depict the GB planes $(h_{nA}k_{nA}l_{nA})/(h_{nB}k_{nB}l_{nB})$. Thus, a GB can be expressed by: $\theta°[h_0k_0l_0](h_{nA}k_{nA}l_{nA})/(h_{nB}k_{nB}l_{nB})$. The orientation of grain A can be displayed by a third-order matrix ($\mathbf{g}_\mathrm{A}$), in which its tri-axial orientation projections are: $\boldsymbol{X}_\mathrm{A} = (r_{\mathrm{A}11}, r_{\mathrm{A}12}, r_{\mathrm{A}13})$, $\boldsymbol{Y}_\mathrm{A} = (r_{\mathrm{A}21}, r_{\mathrm{A}22}, r_{\mathrm{A}23})$ and $\boldsymbol{Z}_\mathrm{A} = (r_{\mathrm{A}31}, r_{\mathrm{A}32}, r_{\mathrm{A}33})$. Those for crystal B, in a third-order matrix ($\mathbf{g}_\mathrm{B}$), can be expressed as: $\boldsymbol{X}_\mathrm{B} = (r_{\mathrm{B}11}, r_{\mathrm{B}12}, r_{\mathrm{B}13})$, $\boldsymbol{Y}_\mathrm{B} = (r_{\mathrm{B}21}, r_{\mathrm{B}22}, r_{\mathrm{B}23})$ and $\boldsymbol{Z}_\mathrm{B} = (r_{\mathrm{B}31}, r_{\mathrm{B}32}, r_{\mathrm{B}33})$. As exhibited in Fig. 2a, the mutual misorientation relationship is virtually a rotation matrix, $\mathbf{R}_\mathrm{AB}$, which can be expressed as follows [53]:

$$\mathbf{R}_\mathrm{AB} = \mathbf{g}_\mathrm{B} \cdot \mathbf{g}_\mathrm{A}^{-1} = \begin{pmatrix} r_{11} & r_{12} & r_{13} \\ r_{21} & r_{22} & r_{23} \\ r_{31} & r_{32} & r_{33} \end{pmatrix}$$

In fact, $\mathbf{R}_\mathrm{AB}$ depicts the rotation of a grain along a specific crystallographic direction, yielding the rotation angle (θ)/axis ($\boldsymbol{c}$) pair. The smallest rotation angle between the two grains is the misorientation angle (or disorientation angle) [28, 54]. And the $\theta/\boldsymbol{c}$ pair can be deduced as below [54]:

$$\theta = \cos^{-1}[\frac{1}{2}(r_{11} + r_{22} + r_{33} - 1)]$$

$$\boldsymbol{c} = [c_1, c_2, c_3] = \frac{1}{2\sin\theta}(r_{32} - r_{23}, r_{13} - r_{31}, r_{21} - r_{12})$$

After acquiring the TKD image (Fig. 2b), the $\theta/\boldsymbol{c}$ pair can be calculated by the software. To recognize the GB planes, both the TKD information and the 3D data reconstruction information need to be combined. Next, an example is applied to illustrate the detailed procedures for identifying the two GB planes with Carine crystallography software.

A crystal of grain A ($\mathbf{g}_{\mathrm{A}}$) is created here. And the stereographic projection map is plotted along $\boldsymbol{Z}_{\mathrm{A}}$ axis (as illustrated in Fig. 2a in local coordinate system). Then, two rotations are applied to bring the GB plane perpendicular to the Y axis. The two rotation angles, $\boldsymbol{\alpha}$ and $\boldsymbol{\beta}$, from which the GB plane normal can be aligned with Y axis, are identified by the combination of the TKD map (Fig. 2b) and the APT atom map (Fig. 2c). The two maps are originally placed at the coincidental position. The atom map is rotated along Y axis until the GB projection appears like a straight line (referred to Fig. 2d) in X-Y plane, and $\boldsymbol{\alpha}$ is the corresponding rotation angle. To obtain $\boldsymbol{\beta}$, the atom map is rotated a second time until this straight-line GB projection is perpendicular to the Y axis.

After doing this, the GB normal direction of grain A is identified as $(6\overline{15})$ for grain A. By creating a crystal similar to grain B ($\mathbf{g}_{\mathrm{B}}$) and performing the similar operation, the GB plane of grain B is identified to be $(25\bar{3})$. Besides, the schematic illustrations of $\boldsymbol{\alpha}$ and $\boldsymbol{\beta}$, as well as the detailed rotation procedures for crystal A, are depicted in Fig. 2a. The TKD analysis from Fig. 2b gives a misorientation information of $52°[\bar{1}01]$. Thus, this general HAGB can be expressed as: $52°[\bar{1}01](6\overline{15})/(25\bar{3})$. The identification process has also been described in [43].

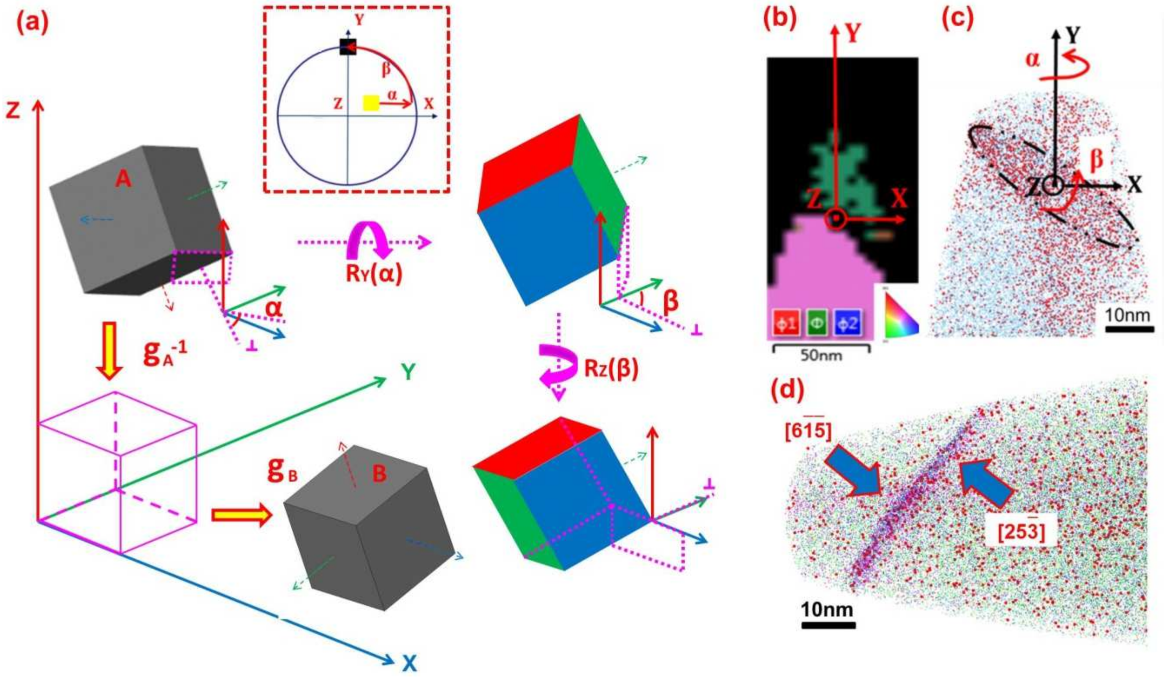

Fig. 2 Schematic illustrations revealing the mutual misorientation (between grain A and grain B) and the identification of GB plane for grains A and B: (a) the mutual misorientation (between the two crystals) and the two rotations ($R_Y(\alpha)$ - the rotation along Y axis by α and $R_Z(\beta)$ - the rotation along Z axis by β, operated in their local coordinate systems) for identifying the GB plane normal direction of grain A; (b) the TKD map exhibiting the GB misorientation information; (c) the reconstructed 3D map with the two rotations (α and β); (d) the GB plane normal directions relative to grains A and B. In (a), "⊥" represents the GB plane normal direction, and the tri-axial orientations of grain A are illustrated by arrows with different colors (X axis in red, Y axis in green and Z axis in blue). In the stereographic projection map, the GB plane direction is illustrated by the yellow square dot, and the final special direction, perpendicular to Y axis, is marked by black square dot.

2.2.2 Calculation of the GB interfacial excess

In Fig. 3, some detected ions after APT analyses are exhibited in a partial mass spectrum. The total concentration of an element is calculated from the proportion of detected ions after identifying each isotope and removing the background information. The uncertainty of the measured concentration of element *i*, if considering only the statistical variation, is given by:

$$\sigma_i = \sqrt{\frac{X_i(1-X_i)}{N_{at}}}$$

where X_i is the measured concentration of solute *i* and N_{at} is the total number of atoms in the analyzed volume.

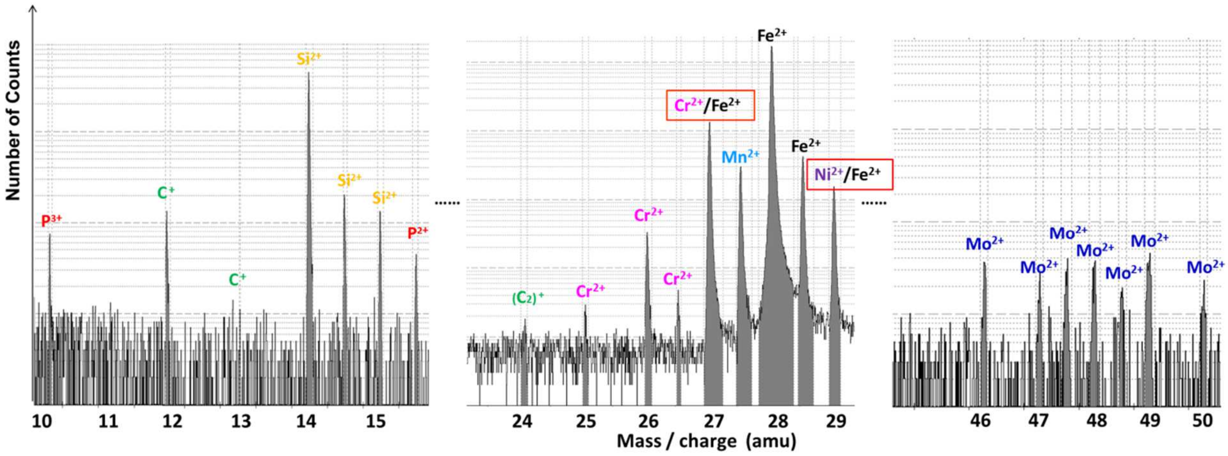

Fig. 3 A partial mass spectrum showing the peak-noise level of some isotopes in ferrite matrix

As shown in Fig. 4a, the GB is visible on the 3D reconstruction map owing to an obvious enrichment of C, P, Mn, Mo and Cr. A sampling cylinder perpendicular to the GB is then selected to plot cumulative profile through the GB. Fig. 4b, c & d plot the cumulative profiles of P, C and Si, respectively. A general method based on the Gibbsian interfacial excess Γ_i [55] was adopted. The Γ_i value (in atoms/nm^2) is defined as:

$$\Gamma_i = \frac{N_i^{\text{excess}}}{\eta \cdot A}$$

in which N_i^{excess} is the number of atoms in excess determined from cumulative profile, η is the detection efficiency of the LEAP and A is the interfacial area of the selected volume. In comparison to C and P, nearly no Si segregation was detected at this GB. Taking into account the uncertainty of each element, the error bar can be measured.

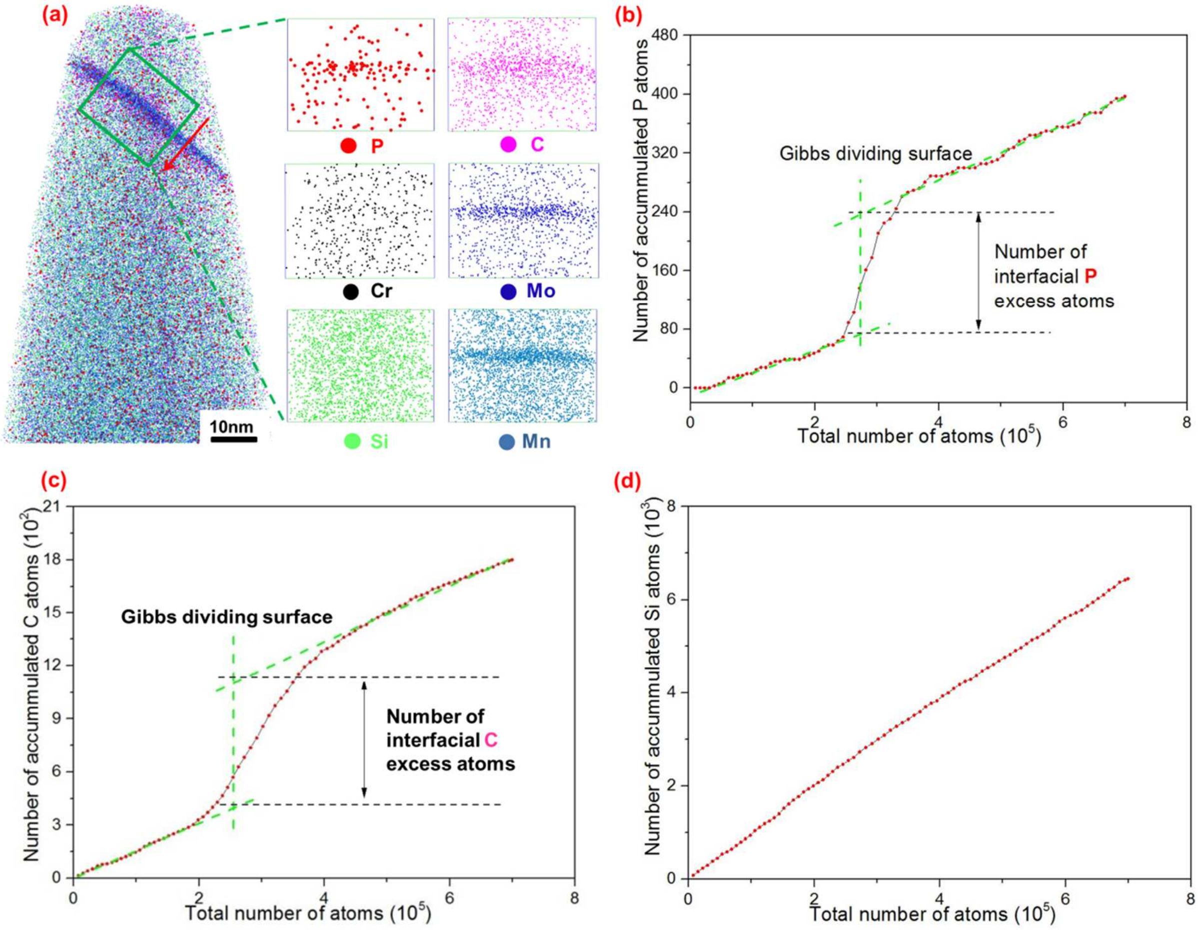

Fig. 4 APT data analyses for: (a) the selected volume (Φ 21.6×16.6 nm^3) exhibiting the element distribution perpendicular across a general HAGB; (b)-(d) the cumulative profiles (corresponding to 16.6 nm) of calculated atoms across the HAGB for P, C and Si elements.

3. Results

3.1 Microstructure characterization and GB identification

The microstructure of the 16MND5 weld is exhibited in Fig. 5a. The inverse pole figure reveals numerous acicular ferrite grains with distinct orientations. These thin grains are arranged in an irregular way, i.e., they intersect with each other. Compared with the "sheaf-like" bainitic ferrite, the acicular ferrite has a "basket-weave" morphology [56]. Similar to bainitic phase transformation, the orientation relationships between parent austenite and acicular ferrite variants are also Nishiyama-Wassermann (N-W) and Kurdjumov-Sachs (K-S) [57]. Numerous carbides are present along the GBs, as shown in Fig. 5b. These carbides have a nanometer size with various shapes: spherical, ellipsoidal, rod-like and plate-like. Two types of carbides, characterized by extensive APT analyses, have the stoichiometry of M_3C (where M consists of Fe, Mn, Mo and Cr [58]) and $M_{2.0\text{-}3.2}C$ (where M contains Fe, Mo and Cr). The Fe concentration is higher than 50 at.% in M_3C carbides (or cementite), while in $M_{2.0\text{-}3.2}C$ carbides, Mo concentration is over 35 at.% and the Fe concentration is less than 30 at.%. Thus, the weld metal mainly has a complex microstructure of acicular ferrite and intergranular carbides (without any intragranular carbides being detected).

LAGB & HAGB is one classification of GB species, in which GBs with a misorientation angle larger than 15° are considered as HAGBs. As exhibited in Fig. 5c, the proportion of HAGB is about 78%, and that of LAGB is about 22%. Among HAGBs, some special ones (Σ3, Σ5, Σ7…) are included. The Σ3 HAGBs are the most favored ones according to the phase transformation orientation relationship [57]. In Fig. 5d, Σ3 special HAGBs represent about 12% of total HAGBs. Due to the presence of numerous carbides, carbide-matrix interfaces are of critical importance. The boundaries are classified as GBs (~22% LAGBs, ~66% general HAGBs and ~12% Σ3 HAGBs) and carbide-ferrite interfaces.

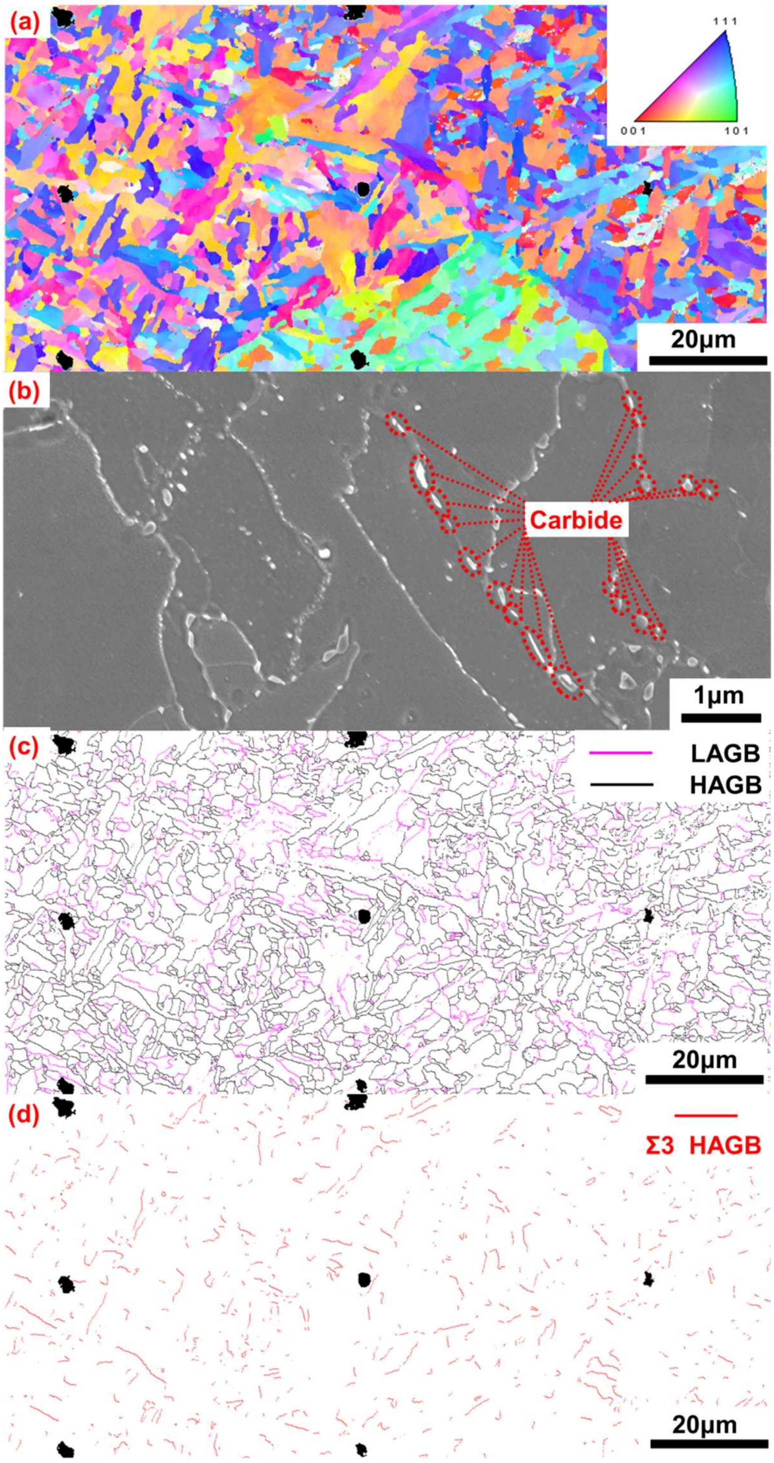

Fig. 5 Characterization of the microstructure and the corresponding GBs: (a) Inverse pole figure map; (b) SEM image showing the intergranular carbides; (c) HAGBs & LAGBs; (d) Σ3 HAGBs. Note that, the 9 black marks are created regularly by FIB milling as complementary signals to identify the relative location of different grains.

3.2 Intergranular segregation and carbide-ferrite interfacial segregation

Table 2 lists the calculated interfacial excess values of identified GBs and interfaces for several chemical species (C, P, Si, Mn, Ni, Cr and Mo). It is inferred that all the LAGBs, general HAGBs, Σ3 HAGBs and carbide-matrix interfaces provide effective sites for the segregation of several elements (P, C, Si, Mn, Ni, Cr and Mo). The segregated P contents are relatively low for all the Σ3 HAGBs and all the $M_{2.0\text{-}3.2}C$ carbide-ferrite interfaces. No depletion of any chemical species was detected.

Table 2 Interfacial excess values (in atoms/nm^2) of the segregated elements for the GBs and interfaces

Element	**P**	**C**	**Si**	**Mn**	**Ni**	**Cr**	**Mo**
LAGB **$5^\circ[6\bar{5}\bar{2}](\bar{5}0\bar{3})/(3\bar{2}0)$**	0.3±0.2	1.1±0.4	0.28±0.05	2.9±0.2	0.8±0.4	0.20±0.04	1.0±0.3
LAGB **$7^\circ[0\bar{1}1](\bar{4}\bar{3}4)/(\bar{6}\bar{5}6)$**	0.3±0.2	1.3±0.4	0.38±0.06	2.1±0.1	0.8±0.2	-	-
LAGB **$12^\circ[104](54\bar{6})/(53\bar{5})$**	0.9±0.3	1.8±0.9	0.5±0.1	4.8±0.5	1.5±0.8	-	0.6±0.4
LAGB **$12^\circ[\bar{3}10](6\bar{3}\bar{1})/(\bar{6}3\bar{1})$**	0.5±0.2	2.0±0.7	0.30±0.04	4.0±0.2	1.4±0.7	-	0.9±0.3
Σ3 HAGB **$59^\circ[111](\bar{6}5\bar{2})/(\bar{5}03)$**	0.2±0.1	0.4±0.1	1.3±0.2	4.1±0.3	2.3±0.3	-	0.4±0.2
Σ3 HAGB **$60^\circ[11\bar{1}](\bar{1}\bar{1}2)/(\bar{3}10)$**	0.2±0.1	1.0±0.6	0.5±0.2	3.2±0.3	1.4±0.7	0.2±0.1	0.5±0.3
Σ3 HAGB **$60^\circ[343](\bar{4}41)/(\bar{4}\bar{1}5)$**	0.3±0.2	1.8±0.6	2.1±0.3	5.3±0.4	1.3±0.3	-	0.6±0.4
Σ3 HAGB **$59.5^\circ[11\bar{1}](4\bar{1}\bar{1})/(\bar{5}22)$**	0.3±0.2	0.8±0.6	1.4±0.2	6.5±0.7	-	-	0.3±0.2
Σ3 HAGB **$60^\circ[111](101)/(01\bar{1})$**	0.07±0.06	1.2±0.4	0.34±0.03	3.5±0.1	0.5±0.3	0.4±0.1	0.7±0.2
Σ3 HAGB **$60^\circ[443](45\bar{1})/(103)$**	0.4±02	1.2±0.6	0.8±0.1	4.0±0.2	0.8±0.4	0.2±0.1	0.6±0.2
General HAGB **$52^\circ[\bar{1}01]\ (6\bar{1}\bar{5})/(25\bar{3})$**	0.4±0.2	4.6±1.2	-	6.5±0.4	2.0±0.5	0.3±0.1	3.4±1.5
General HAGB **$49^\circ[403](010)/(35\bar{5})$**	0.6±0.3	5.0±1.2	0.5±0.1	5.8±0.3	1.1±0.5	0.3±0.1	1.8±0.9
General HAGB **$49.5^\circ[\bar{1}10](\bar{4}2\bar{5})/(5\bar{4}2)$**	0.3±0.1	4.1±1.4	1.3±0.2	7.1±0.4	-	0.5±0.2	1.7±0.9
General HAGB **$54^\circ[2\bar{4}\bar{3}](1\bar{1}0)/(1\bar{5}0)$**	1.0±0.5	3.7±1.0	0.8±0.1	5.6±0.5	0.8±0.4	-	1.4±1.0
General HAGB **$52^\circ[\bar{3}3\bar{1}](\bar{5}43)/(65\bar{5})$**	0.8±0.2	5.3±1.1	1.9±0.2	6.6±0.3	1.8±0.9	0.4±0.1	2.8±1.0
General HAGB **$54^\circ[\bar{5}25](\bar{1}\bar{1}\bar{2})(0\bar{3}1)$**	0.11±0.02	6.7±1.6	-	1.7±0.1	-	0.4±0.1	1.5±0.4
General HAGB **$54^\circ[433](5\bar{5}2)/(6\bar{3}\bar{1})$**	0.9±0.3	3.3±0.9	0.54±0.07	4.8±0.3	1.7±1.0	0.3±0.1	2.7±0.7
Cementite-ferrite Interface 1	0.8±0.4	-	0.9±0.4	-	0.8±0.1	-	-

Cementite-ferrite Interface 2	0.06±0.05	-	-	-	-	-	-
Cementite-ferrite Interface 3	0.2±0.1	-	-	-	-	-	-
Cementite-ferrite Interface 4	0.2±0.1	-	-	-	-	-	-
Cementite-ferrite Interface 5	0.03±0.02	-	2.8±0.5	-	-	-	-
Cementite-ferrite Interface 6	0.4±0.2	-	-	-	0.3±0.1	-	-
Cementite-ferrite Interface 7	0.7±0.2	-	-	-	-	-	-
Cementite-ferrite Interface 8	0.2±0.1	-	-	-	0.6±0.3	-	-
Cementite-ferrite Interface 9	0.8±0.3	-	-	-	0.6±0.3	-	-
M$_{2.0\text{-}3.2}$C carbide-ferrite Interface 1	0.2±0.1	-	0.38±0.01	4.0±0.2	-	-	-
M$_{2.0\text{-}3.2}$C carbide-ferrite Interface 2	0.10±0.04	-	1.7±0.1	5.5±0.2	1.6±0.8	-	-
M$_{2.0\text{-}3.2}$C carbide-ferrite Interface 3	0.14±0.09	-	0.3±0.1	2.0±0.2	0.6±0.3	-	-

Notes: "-" means that no obvious segregation or depletion is detected.

The peak and average values of P interfacial excess for each GB and interface types are listed in Table 3. The average values of segregated P contents are higher in LAGBs and general HAGBs than in other boundary types. The variation of the segregated P content from one carbide-ferrite interface to another could be attributed to their distinct lattice coherencies between carbide and ferrite matrix.

Table 3 Interfacial excess values (in atoms/nm^2) of P for the identified boundaries. For each type of GB or interface, the number of investigated features is given into parenthesis.

	GBs			**Interfaces**	
	LAGBs (4)	**General HAGBs (7)**	**Σ3 HAGBs (6)**	**Cementite-ferrite interfaces (9)**	**M$_{2.0\text{-}3.2}$C carbide-ferrite interfaces (3)**
Peak	0.9±0.3	1.0±0.5	0.4±0.2	0.8±0.4 (or 0.8±0.3)	0.2±0.1
Average	0.5±0.2	0.6±0.2	0.2±0.1	0.4±0.2	0.15±0.07

As exhibited in Fig. 6, another LAGB $3°[\bar{5}\bar{2}3](5\bar{4}\bar{3})/(3\bar{3}4)$ was also investigated (not reported in Table 2 & 3). It is clear that this tilted LAGB is composed of an array of parallel accommodation edge dislocations. These dislocation lines are easily identified because of the segregation of several elements (C, Mo, P, Cr, Mn and V). Similar observations were reported in neutron-irradiated Fe-Cr model alloys [59, 60]. The Burgers vector was measured using the expression [5]: $|\mathbf{b}_{\mathrm{exp}}| = 2 \cdot d \cdot \sin(\theta/2) \approx d \cdot \sin\theta$, where d is the distance between two intrinsic dislocations measured from the 3D reconstruction map (d = (5.0±0.2) nm) and θ is the misorientation angle acquired from the TKD map ($\theta = 3°$). In this case, $|\mathbf{b}_{\mathrm{exp}}|$ was found to be (0.26±0.01) nm. In BCC iron, the theoretical value of Burgers vector is given by $|\mathbf{b}_{\mathrm{the}}| = \sqrt{3}/2$ a. With a = 0.286 nm (lattice parameter), $|\mathbf{b}_{\mathrm{the}}|$ is about 0.25 nm, in excellent agreement with $|\mathbf{b}_{\mathrm{exp}}|$ value. Some Mo, Cr, V and C-enriched features appear along these edge dislocations. For this LAGB, the solute segregation was not quantified and thus not reported in Table 2 & 3 because of the presence of some Mo, Cr, V and C-enriched features.

Besides, a dislocation with a clear Mo and C segregation also appears near the LAGB (shown in Fig. 6). In contrast, the P segregation is not so obvious. It seems that, in the 16MND5 weld, P segregation at dislocations is not as obvious as that at GBs or carbide-ferrite interfaces.

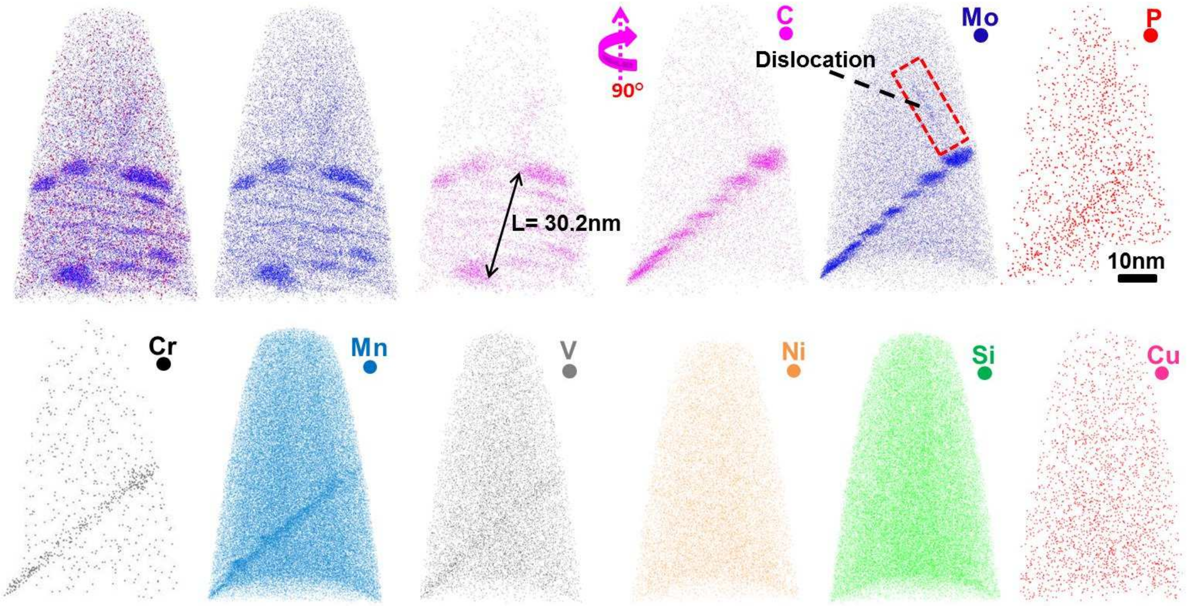

Fig. 6 3D reconstruction of a LAGB 3°[$\bar{5}\bar{2}3$]($\bar{5}\bar{4}3$)/($3\bar{3}4$) with a dislocation present near it. The tilted LAGB is composed of some primary edge dislocations spaced at an average distance d = L/6 = (5.0±0.2) nm. The dislocation near the LAGB is delineated.

3.3 Interstitial segregation and substitutional segregation

The segregation level at a GB is correlated with both its Gibbs free energy and structure. The GB with higher free energy promotes stronger segregation. For the present steel with a multicomponent composition system, the intergranular segregation from all chemical species is considered in a comprehensive way to clarify the GB segregation anisotropy with regard to the 5 parameters of a GB.

It is acknowledged that Si, Cr, Mo, Ni and Mn favor substitutional segregation while C enhances interstitial segregation. The calculated values of total interfacial excess values of substitutional elements (Si, Cr, Mo, Ni and Mn) are plotted in Fig. 7a. It appears that the segregated level of total substitutional elements is higher in general HAGBs than in LAGBs or Σ3 HAGBs. The average values for LAGBs, Σ3 HAGBs and general HAGBs are (5.8±1.3), (7.2±1.1) and (9.7±1.9) atoms/nm^2, respectively. In practical steels, a Σ3 HAGB possesses a specific deviation angle from an ideal Σ3 HAGBs, thus favoring a considerable segregation of several elements. The substitutional segregation level of Σ3 HAGBs is quite high, which makes these Σ3 HAGBs not real special from an energetic perspective. The substitutional segregation level of Σ3 HAGB 60°[343] $(\bar{4}41)/(\bar{4}\bar{1}5)$, with a deviation angle of 8.5°, seems to be competitive with that of a random HAGB.

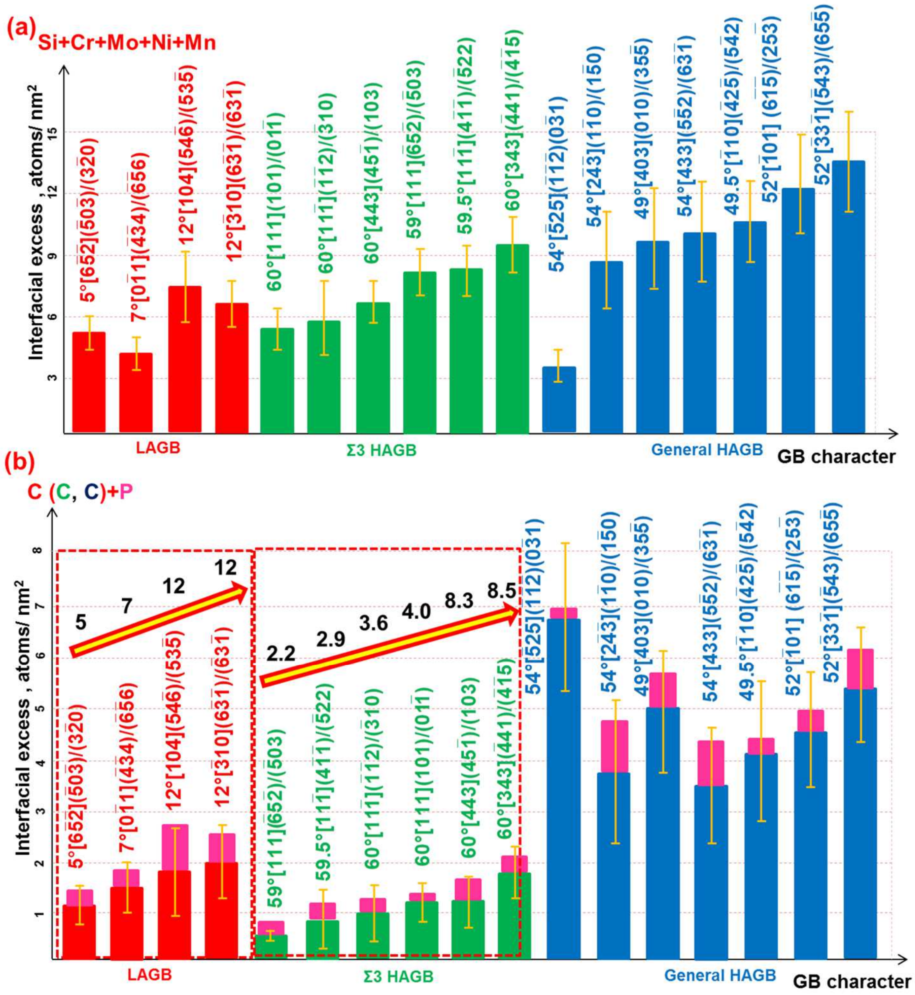

Fig. 7 Variation of total interfacial excess values with GB type for: (a) substitutional segregation (Si+Cr+Mo+Ni+Mn); (b) interstitial segregation of C (+ P, in black). Note that, different GB types are marked with distinct colors. Particularly, the values of misorientation angles for LAGBs, as well as the deviation angles for Σ3 HAGB, are marked in b along the arrow plotting the increasing trend.

There is a variation of the total interfacial excess values among Σ3 HAGBs and among general HAGBs. Probably, besides the Σ value, other factors are also responsible for the substitutional segregation behavior. In the present study, this variation could be explained by an influence of the two adjoining GB planes. It seems that if the GB plane has low Miller-index values, the segregation level will be low. This is the case in the Σ3 HAGBs 60°[111](101)/($01\bar{1}$) and 60°[$11\bar{1}$]($\bar{1}\bar{1}2$)/($\bar{3}10$) among all the Σ3 HAGBs, and the case in the general HAGB 54°[$\bar{5}25$]($\bar{1}\bar{1}2$)($0\bar{3}1$) among all the general HAGBs. It is reported that the low

Miller-index GB planes tend to possess low energy [10, 61, 62]. When the adjoining two GB planes tend to own high Miller-index values, the segregation level will be high. This rule, consistent with previous experimental results [10], perfectly matches our observations for substitutional segregation. Recent research on an AISI 304L stainless steel [63] also reported that its corrosion behavior is dominated by GB plane for low-Σ CSL GBs and random HAGBs. A possible explanation for the GB plane influence lies in the presence of large excess volume for HAGBs with a high Miller-index value [64, 65]. The GB excess volume describes the expansion ability induced by the presence of a GB in polycrystalline materials based on hard sphere model [66]. A low Miller-index GB plane was reported to be associated with low-energy and small amount of volume expansion in BCC metals [67].

As shown in Fig. 7b (if not taking into consideration the black bar representative of P), the interfacial excess values of C are higher in all the general HAGBs than those in the LAGBs or Σ3 HAGBs. The segregated C content in all the Σ3 HAGBs is much lower in comparison to all general HAGBs, which renders Σ3 HAGBs quite special with low energy. Moreover, the segregated C content among LAGBs (or Σ3 HAGBs) varies with the misorientation angle (or the deviation angle). With the increased dislocation density, the segregated C content increases with misorientation angle in the range 5-12°. For LAGBs with a misorientation of 12° (12°$[104](54\bar{6})/(53\bar{5})$ and 12°$[\bar{3}10](6\bar{3}\bar{1})/(\bar{6}3\bar{1})$), the interfacial excess values of P and C can go up to 0.9±0.3 and 2.0±0.7 atoms/nm^2, respectively. Similarly, the C segregation level rises gradually with the increase of deviation angle in the range 2.2-8.5° (shown in Fig. 6b).

Notably, the segregation mechanism of P may be more complex. Density Functional Theory (DFT) calculations (at 0 K) in α-Fe revealed that the segregation energy for a P atom placed in substitutional position is lower than that in its interstitial position. According to this, some research argued that some Fe atoms are substituted by P atoms at a GB [68-70]. Also, it was predicted that P segregates interstitially at high temperature based on the enthalpy-entropy compensation effect [71, 72]. Recently, Pavel Lejček revisited the data based on thermodynamic calculations and proposed that, with the increase of temperature, there should be an alteration of P segregation position at a GB in α-Fe: at 0 K, substitutional segregation of P is preferred, while interstitial segregation occurs at high temperature (exceeding about 650 K). For practical interest (with a temperature above 700 K), the interstitial segregation of P is explained by entropy driven transition of the segregation site [73]. According to this, the probable segregation position of P is interstitial in the present steel.

If we consider (C+P) as interstitial segregants, it seems that the cumulative segregation profile (for C+P as shown in Fig. 7b) does not change a lot, and that the cumulative segregation level increases with misorientation angle (or deviation angle). It is reported that there is a possible site competition between C and P, in which C atoms preferentially occupy the sites at the GB, leaving less free sites for P segregation [8, 41, 74]. There is a much higher segregation level for C than P for all GB types. Here, P is not separated individually considering the potential site competition with C. To make a pertinent conclusion that P segregates interstitially at high temperature, it is better to investigate a controlled composition system with high-P but low-C to limit the segregated C content.

Though, in the current analysis, both P and C prefer interstitial segregation at GBs, they bring in opposite effects. P is deleterious for mechanical property with particular weakening effect on the cohesive strength between crystalline grains, while intergranular C decoration is generally believed to be positive on GB cohesion [75, 76]. The C segregation at GBs suppresses the intergranular fracture induced by P segregation, and this could be explained by: (i) the enhanced GB cohesion by segregated C as its inherent effect [77] and (ii) the reduced P segregation in association with the site competition mechanism that C atoms can replace the P atoms at GBs [8].

We interpret the whole GB crystallography as well as the segregants in a comprehensive way. In general, both the interstitial and substitutional segregation levels are high for the random HAGBs (except the case $54°[\bar{5}25](\bar{1}\bar{1}\bar{2})(0\bar{3}1)$). Among all the general HAGBs (or Σ3 HAGBs), the variation of substitutional segregation level can be explained by the GB planes, as discussed above. Typically, a GB with a misorientation angle smaller than 15° is considered as a LAGB. According to the Frank-Bilby theory, a LAGB can be regarded as an array of dislocations and the increase of misorientation angle can be released by the enhanced dislocation density as well as the increased energy [78]. The increasing trend of interstitial segregation level with misorientation angle (or deviation angle) in LAGBs (or Σ3 HAGBs) is also clear.

4. Conclusions

1) For the present research, a joint chemical characterization and crystallographic identification were acquired on the same sample at the same location in a 16MND5 weld, and the intergranular segregation behaviors were correlated to the 5 parameters. This correlative EBSD/TKD/APT methodology opens a feasible way to quantify the GB segregation with regard to its 5-parameter crystallography for polycrystalline materials with a complex composition system.

2) The microstructure of the steel is mainly composed of acicular ferrite and intergranular carbides. Two types of carbides, cementite carbide and $M_{2.0\text{-}3.2}C$ carbide, were detected in the present steel. The typical boundaries in the experimental weld metal are classified as GBs and carbide-ferrite interfaces. A classification of the GBs is ~22% LAGBs, ~66% random HAGBs and ~12% Σ3 HAGBs, and the carbide-ferrite interfaces include cementite-ferrite interfaces and $M_{2.0\text{-}3.2}C$ carbide-ferrite interfaces.

3) There is an obvious segregation of one element or several chemical species (C, P, Mn, Mo, Cr, Si and Ni) for all boundary types. The general HAGBs possess a high segregation level for both interstitial and substitutional elements. Among all the general HAGBs (or Σ3

HAGBs), there could be a significant influence of the two adjoining GB planes on substitutional segregation. If a GB has two low Miller-index planes, the segregation level is found to be low; and vice versa.

4) Interstitial segregation level increases with misorientation angle for LAGBs, and it also increases with deviation angle for Σ3 HAGBs. P, as well as C, is thought to favor interstitial segregation. The average values of segregated P contents are higher in LAGBs and general HAGBs than in other GB types or interfaces. Besides, the carbide-ferrite interfaces provide effective sites for P segregation. It seems that P segregation at dislocations is not as obvious as that at GBs or carbide-ferrite interfaces.

Acknowledgement

This work was performed on the GENESIS platform, financially supported by Centre National de la Recherche Scientifique (CNRS) belonging to the project entitled “Investissements d’avenir” with a reference number ANR-11-EQPX-0020. This work is part of the EM2VM Joint Laboratory Study and Modeling of the Microstructure for Ageing of Materials. This work was supported by the MAI-sn (Materials Ageing Institute-Scientific Network (http://themai.org/scientific-network).

The authors also owe their sincere gratitude to Prof. Didier Blavette for the fruitful discussions.

Research Data

Data not available / Data will be made available on request.

References:

[1] M.A. Gibson, C.A. Schuh, Segregation-induced changes in grain boundary cohesion and embrittlement in binary alloys, Acta Mater. 95 (2015) 145-155.

[2] E.A. Kuleshova, B.A. Gurovich, Z.V. Lavrukhina, D.A. Maltsev, S.V. Fedotova, A.S. Frolov, G.M. Zhuchkov, Study of the flux effect nature for VVER-1000 RPV welds with high nickel content, J. Nucl. Mater. 483 (2017) 1-12.

[3] P. Lejček, M. Šob, V. Paidar, Interfacial segregation and grain boundary embrittlement: an overview and critical assessment of experimental data and calculated results, Prog. Mater. Sci. 87 (2017) 83-139.

[4] Y.I. Shtrombakh, B.A. Gurovich, E.A. Kuleshova, D.A. Maltsev, S.V. Fedotova, A.A. Chernobaeva, Thermal ageing mechanisms of VVER-1000 reactor pressure vessel steels, J. Nucl. Mater. 452 (1-3) (2014) 348-358.

[5] P. Lejcek. Grain boundary segregation in metals, Springer Science & Business Media, Berlin, 2010.

[6] C. Naudin, J.M. Frund, A. Pineau, Intergranular fracture stress and phosphorus grain boundary segregation of a Mn-Ni-Mo steel, Scripta Mater. 40 (9) (1999) 1013-1019.

[7] B.A. Gurovich, E.A. Kuleshova, Y.A. Nikolaev, Y.I. Shtrombakh, Assessment of relative contributions from different mechanisms to radiation embrittlement of reactor pressure vessel steels, J. Nucl. Mater. 246 (2-3) (1997) 91-120.

[8] H. Erhart, H.J. Grabke, Equilibrium segregation of phosphorus at grain boundaries of Fe-P, Fe-C-P, Fe-Cr-P, and Fe-Cr-C-P Alloys, Met. Sci. 15 (9) (1981) 401-408.

[9] M. Guttmann, Equilibrium segregation in a ternary solution: A model for temper embrittlement, Surf. Sci. 53 (1) (1975) 213-227.

[10] S. Suzuki, K. Abiko, H. Kimura, Phosphorus segregation related to the grain boundary structure in an Fe-P alloy, Scripta Metall. Mater. 15 (10) (1981) 1139-1143.

[11] T. Ogura, C.J. McMahon, H.C. Feng, V. Vitek, Structure-dependent intergranular segregation of phosphorus in austenite in a Ni-Cr steel, Acta Metall. Mater. 26 (9) (1978) 1317-1330.

[12] G.O. Williams, V. Randle, J.R. Cowan, P. Spellward, The role of misorientation and phosphorus content on grain growth and intergranular fracture in iron-carbon-phosphorus alloys, J. Microsc. 213 (3) (2004) 321-327.

[13] J. Kameda, C.J. McMahon, Solute segregation and brittle fracture in an alloy steel, Metall. Mater. Trans. A, 11 (1) (1980) 91-101.

[14] V.J. Keast, D.B. Williams, Grain boundary chemistry, Curr. Opin. Solid St. M. 5 (2001) 23-30.

[15] P. Doig, P. Flewitt, The influence of temper embrittlement on the stress corrosion susceptibility of Fe-3 wt.% Ni alloys, Acta Metall. Mater. 26 (8) (1978) 1283-1291.

[16] D. Blavette, P. Duval, L. Letellier, M. Guttmann, Atomic-scale APFIM and TEM investigation of grain boundary microchemistry in Astroloy nickel base superalloys, Acta Mater. 44 (12) (1996) 4995-5005.

[17] K. Stiller, Grain boundary chemistry in nickel base alloy 600, Le Journal de Physique Colloques 50 (C8) (1989) 329-334.

[18] D.B. Williams, C.B. Carter, High Energy-Loss Spectra and Images, Transmission Electron Microsc.

(2009) 715-739.

[19] M.K. Miller, R.G. Forbes, Atom-probe tomography: the local electrode atom probe, Springer Science & Business Media, New York, 2014.

[20] T.L. Martin, A.J. London, B. Jenkins, S.E. Hopkin, J.O. Douglas, P.D. Styman, P.A. Bagot, M.P. Moody, Comparing the consistency of atom probe tomography measurements of small-scale segregation and clustering between the LEAP 3000 and LEAP 5000 instruments, Microsc. Microanal. 23 (2) (2017) 227-237.

[21] M. Herbig, D. Raabe, Y.J. Li, P. Choi, S. Zaefferer, S. Goto, Atomic-scale quantification of grain boundary segregation in nanocrystalline material, Phys. Rev. Lett. 112 (12) (2014) 126103.

[22] V. Randle, Application of EBSD to the analysis of interface planes: evolution over the last two decades, J. of Microsc. 230 (3) (2008) 406-413.

[23] A.D. Rollett, S. Lee, R. Campman, G.S. Rohrer, Three-dimensional characterization of microstructure by electron back-scatter diffraction, Annu. Rev. Mater. Res. 37 (2007) 627-658.

[24] K. Babinsky, W. Knabl, A. Lorich, R. De Kloe, H. Clemens, S. Primig, Grain boundary study of technically pure molybdenum by combining APT and TKD, Ultramicroscopy, 159 (2015) 445-451.

[25] S. Mandal, K.G. Pradeep, S. Zaefferer, D. Raabe, A novel approach to measure grain boundary segregation in bulk polycrystalline materials in dependence of the boundaries' five rotational degrees of freedom, Scripta Mater. 81 (2014) 16-19.

[26] K. Babinsky, R. De Kloe, H. Clemens, S. Primig, A novel approach for site-specific atom probe specimen preparation by focused ion beam and transmission electron backscatter diffraction, Ultramicroscopy, 144 (2014) 9-18.

[27] L. Yao, S.P. Ringer, J.M. Cairney, M.K. Miller, The anatomy of grain boundaries: Their structure and atomic-level solute distribution, Scripta Mater. 69 (8) (2013) 622-625.

[28] S. Baik, M.J. Olszta, S.M. Bruemmer, D.N. Seidman, Grain-boundary structure and segregation behavior in a nickel-base stainless alloy, Scripta Mater. 66 (10) (2012) 809-812.

[29] M. Herbig, Spatially correlated electron microscopy and atom probe tomography: Current possibilities and future perspectives, Scripta Mater. 148 (2018) 98-105.

[30] D. Raabe, M. Herbig, S. Sandlöbes, Y. Li, D. Tytko, M. Kuzmina, D. Ponge, P. Choi, Grain boundary segregation engineering in metallic alloys: A pathway to the design of interfaces, Curr. Opin. Solid St. M. 18 (4) (2014) 253-261.

[31] J. May, H. Hein, E. Altstadt, F. Bergner, H.W. Viehrig, A. Ulbricht, R. Chaouadi, B. Radiguet, S. Cammelli, H. Huang. FP7 project LONGLIFE: Treatment of long-term irradiation embrittlement effects in RPV safety assessment, Third International Conference on Nuclear Power Plant Life Management, Salt Lake City, USA (2012) 14-18.

[32] M.K. Miller, K.F. Russell, Embrittlement of RPV steels: An atom probe tomography perspective, J. Nucl. Mater. 371 (1-3) (2007) 145-160.

[33] G. Kuri, S. Cammelli, C. Degueldre, J. Bertsch, D. Gavillet, Neutron induced damage in reactor pressure vessel steel: An X-ray absorption fine structure study, J. Nucl. Mater. 385 (2) (2009) 312-318.

[34] M.K. Miller, K.F. Russell, J. Kocik, E. Keilova, Embrittlement of low copper VVER 440 surveillance samples neutron-irradiated to high fluences, J. Nucl. Mater. 282 (1) (2000) 83-88.

[35] M.K. Miller, K.F. Russell, M.A. Sokolov, R.K. Nanstad, APT characterization of irradiated high nickel RPV steels, J. Nucl. Mater. 361 (2-3) (2007) 248-261.

[36] M.K. Miller, K.F. Russell, M.A. Sokolov, R.K. Nanstad, Atom probe tomography characterization of radiation-sensitive KS-01 weld, J. Nucl. Mater. 320 (3) (2003) 177-183.

[37] B.A. Gurovich, E.A. Kuleshova, Y.I. Shtrombakh, D.Y. Erak, A.A. Chernobaeva, O.O. Zabusov, Fine structure behaviour of VVER-1000 RPV materials under irradiation, J. Nucl. Mater. 389 (3) (2009) 490-496.

[38] B.A. Gurovich, E.A. Kuleshova, Y.I. Shtrombakh, O.O. Zabusov, E.A. Krasikov, Intergranular and intragranular phosphorus segregation in Russian pressure vessel steels due to neutron irradiation, J. Nucl. Mater. 279 (2-3) (2000) 259-272.

[39] E.A. Kuleshova, B.A. Gurovich, Z.V. Lavrukhina, M.A. Saltykov, S.V. Fedotova, A.N. Khodan, Assessment of segregation kinetics in water-moderated reactors pressure vessel steels under long-term operation, J. Nucl. Mater. 477 (2016) 110-122.

[40] P. Ševc, J. Janovec, M. Koutnik, A. Výrostková, Equilibrium grain boundary segregation of phosphorus in 2.6 Cr-0.7 Mo-0.3 V steels, Acta Metall. Mater. 43 (1) (1995) 251-258.

[41] M. Guttmann, P. Dumoulin, M. Wayman, The thermodynamics of interactive co-segregation of phosphorus and alloying elements in iron and temper-brittle steels, Metall. Trans. A 13 (10) (1982) 1693-1711.

[42] P. Dumoulin, M. Guttmann, The influence of chemical interactions between metallic and metalloid solutes on their segregation in α-Fe I: Co-segregation at free surface studied by Auger electron

spectroscopy, Mater. Sci. Eng. 42 (1980) 249-263.

[43] A. Akhatova, F. Christien, V. Barnier, B. Radiguet, E. Cadel, F. Cuvilly, P. Pareige, Investigation of the dependence of phosphorus segregation on grain boundary structure in Fe-P-C alloy: cross comparison between Atom Probe Tomography and Auger Electron Spectroscopy, Appl. Surf. Sci. 463 (2019) 203-210.

[44] D.G. Brandon, The structure of high-angle grain boundaries, Acta Metall. Mater. 14 (1966) 1479-1484.

[45] Y. Tu, H. Takamizawa, B. Han, Y. Shimizu, K. Inoue, T. Toyama, F. Yano, A. Nishida, Y. Nagai, Influence of laser power on atom probe tomographic analysis of boron distribution in silicon, Ultramicroscopy, 173 (2017) 58-63.

[46] J.M. Hyde and C.A. English, “Microstructural Characterisation Techniques for Mechanistic Understanding of Irradiation Damage”, in “Irradiation Embrittlement of Reactor Pressure Vessels (RPVs) in Nuclear Power Plants”, Elsevier, Oxford, 2014.

[47] R.K. Marceau, P. Choi, D. Raabe, Understanding the detection of carbon in austenitic high-Mn steel using atom probe tomography, Ultramicroscopy, 132 (2013) 239-247.

[48] M. Müller, B. Gault, G. Smith, C. Grovenor. Accuracy of pulsed laser atom probe tomography for compound semiconductor analysis., Journal of Physics: Conference Series, IOP Publishing, 326 (1) (2011) 12031.

[49] B. Gault, M. Müller, A. La Fontaine, M.P. Moody, A. Shariq, A. Cerezo, S.P. Ringer, G. Smith, Influence of surface migration on the spatial resolution of pulsed laser atom probe tomography, J Appl Phys, 108 (4) (2010) 044904.

[50] D.J. Larson, T.J. Prosa, R.M. Ulfig, B.P. Geiser, T.F. Kelly, Local electrode atom probe tomography, Springer Science & Business Media, New York, 2013.

[51] B. Gault, F. De Geuser, L.T. Stephenson, M.P. Moody, B.C. Muddle, S.P. Ringer, Estimation of the reconstruction parameters for atom probe tomography, Microsc. Microanal. 14 (4) (2008) 296-305.

[52] P. Bas, A. Bostel, B. Deconihout, D. Blavette, A general protocol for the reconstruction of 3D atom probe data, Appl. Surf. Sci. 87 (1995) 298-304.

[53] H. Grimmer, W.T. Bollmann, D.H. Warrington, Coincidence-site lattices and complete pattern-shift in cubic crystals, Acta Crystall. A - Crys. 30 (2) (1974) 197-207.

[54] W. Bollmann. Crystal defects and crystalline interfaces, Springer Science & Business Media, Berlin, 2012.

[55] B.W. Krakauer, D.N. Seidman, Absolute atomic-scale measurements of the Gibbsian interfacial excess of solute at internal interfaces, Phys. Rev. B 48 (9) (1993) 6724-6727.

[56] R.A. Farrar, P.L. Harrison, Acicular ferrite in carbon-manganese weld metals: an overview, J. Mater. Sci. 22 (11) (1987) 3812-3820.

[57] S.S. Babu, H. Bhadeshia, Stress and the acicular ferrite transformation, Mater. Sci. Eng. A - Struct. 156 (1) (1992) 1-9.

[58] A.J. Clarke, M.K. Miller, R.D. Field, D.R. Coughlin, P.J. Gibbs, K.D. Clarke, D.J. Alexander, K.A. Powers, P.A. Papin, G. Krauss, Atomic and nanoscale chemical and structural changes in quenched and tempered 4340 steel, Acta Mater. 77 (2014) 17-27.

[59] V. Kuksenko, C. Pareige, C. Genevois, P. Pareige, Characterisation of Cr, Si and P distribution at dislocations and grain-boundaries in neutron irradiated Fe-Cr model alloys of low purity, J. Nucl. Mater. 434 (1-3) (2013) 49-55.

[60] V. Kuksenko, C. Pareige, P. Pareige, Cr precipitation in neutron irradiated industrial purity Fe-Cr model alloys, J. Nucl. Mater. 432 (1-3) (2013) 160-165.

[61] T. Ogura, T. Watanabe, S. Karashima, T. Masumoto, Dependence of phosphorus segregation on grain boundary crystallography in an Fe-Ni-Cr alloy, Acta Metall. Mater. 35 (7) (1987) 1807-1814.

[62] H. Ichinose, Y. Ishida, Observation of [110) tilt boundary structures in gold by high resolution HVEM, Philos. Mag. A 43 (5) (1981) 1253-1264.

[63] D.Y. An, T.A. Griffiths, P. Konijnenberg, S. Mandal, Z. Wang, S. Zaefferer, Correlating the five parameter grain boundary character distribution and the intergranular corrosion behavior of a stainless steel using 3D orientation microscopy based on mechanical polishing serial sectioning, Acta Mater. 156 (2018) 297-309.

[64] C. Li, D.B. Williams, The relationship between grain-boundary structure and segregation in a rapidly solidified Fe-P alloy, Philos. Mag. 85 (18) (2005) 2023-2032.

[65] J.J. Bean, K.P. McKenna, Origin of differences in the excess volume of copper and nickel grain boundaries, Acta Mater. 110 (2016) 246-257.

[66] H.J. Frost, F. Spaepen, Hard sphere models for the structure of grain boundaries, Le Journal de Physique Colloques 43(C6) (1982) 73-82.

[67] D. Wolf, Structure and energy of general grain boundaries in bcc metals, J. Appl. Phys. 69 (1) (1991) 185-196.

[68] M. Hashimoto, Y. Ishida, R. Yamamoto, M. Doyama, Atomistic studies of grain boundary segregation in Fe-P and Fe-B alloys - I. Atomic structure and stress distribution, Acta Metall. Mater. 32 (1) (1984) 1-11.

[69] M. Yamaguchi, First-principles study on the grain boundary embrittlement of metals by solute segregation: Part I. iron (Fe)-solute (B, C, P, and S) systems, Metall. Mater. Trans. A, 42 (2) (2011) 319-329.

[70] M. Yuasa, M. Mabuchi, First-principles study on enhanced grain boundary embrittlement of iron by phosphorus segregation, Mater. Trans. 52 (7) (2011) 1369-1373.

[71] E. Wachowicz, A. Kiejna, Effect of impurities on structural, cohesive and magnetic properties of grain boundaries in α-Fe, Model. Simul. Mater. Sc. 19 (2) (2011) 25001.

[72] R. Wu, A.J. Freeman, G.B. Olson, First principles determination of the effects of phosphorus and boron on iron grain boundary cohesion, Science, 265 (5170) (1994) 376-380.

[73] P. Lejček, S. Hofmann, Interstitial and substitutional solute segregation at individual grain boundaries of α-iron: data revisited, J. Phys. Condens. Mat. 28 (6) (2016) 64001.

[74] Z. Lu, R.G. Faulkner, N. Sakaguchi, H. Kinoshita, H. Takahashi, P. Flewitt, Effect of hafnium on radiation-induced inter-granular segregation in ferritic steel, J. Nucl. Mater. 351 (1-3) (2006) 155-161.

[75] R. Wu, A.J. Freeman, G.B. Olson, Effects of carbon on Fe-grain-boundary cohesion: First-principles determination, Phys. Rev. B, 53 (11) (1996) 7504-7509.

[76] M.P. Seah, Adsorption-induced interface decohesion, Acta Metall. Mater. 28 (7) (1980) 955-962.

[77] K. Abiko, S. Suzuki, H. Kimura, Effect of Carbon on the Toughness and Fracture Mode of Fe-P Alloys, T. Jpn. I. Met. 23 (2) (1982) 43-52.

[78] B.A. Bilby, R. Bullough, E. Smith. Continuous distributions of dislocations: a new application of the methods of non-Riemannian geometry, Proc. R. Soc. Lond. A 231 (1185) (1955) 263-273.